

# Wetting, roughness and flow boundary conditions.

Olga I. Vinogradova<sup>1,2</sup> and Aleksey V. Belyaev<sup>1,3</sup>

<sup>1</sup> A.N. Frumkin Institute of Physical Chemistry and Electrochemistry, Russian Academy of Sciences, 31 Leninsky Prospect, 119991 Moscow, Russia

<sup>2</sup> ITMC and DWI, RWTH Aachen, Pauwelsstr. 8, 52056 Aachen, Germany

<sup>3</sup> Physics Department, M.V. Lomonosov Moscow State University, 119991 Moscow, Russia

E-mail: oivinograd@yahoo.com

**Abstract.** We discuss how the wettability and roughness of a solid impacts its hydrodynamic properties. We see in particular that hydrophobic slippage can be dramatically affected by the presence of roughness. Owing to the development of refined methods for setting very well-controlled micro- or nanotextures on a solid, these effects are being exploited to induce novel hydrodynamic properties, such as giant interfacial slip, superfluidity, mixing, and low hydrodynamic drag, that could not be achieved without roughness.

Submitted to: *J. Phys.: Condens. Matter*

## 1. Introduction

Fluid mechanics is one of the oldest and useful of the ‘exact’ sciences. For hundreds of years it has relied upon the no-slip boundary condition at a solid-liquid interface, that was applied successfully to model many macroscopic experiments [1]. However, the problem is not that simple and has been revisited recent years. One reason for such a strong interest in ‘old’ problem is purely fundamental. The no-slip boundary condition is an assumption that cannot be derived from first principles even for a molecularly smooth hydrophilic [the contact angle (fixed by the chemical nature of a solid) lies between  $0^\circ$  and  $90^\circ$ ] surface. Therefore, the success of no-slip postulate may not always reflect its accuracy but in fact rather the insensitivity of the experiment. Another reason for current interest to flow boundary conditions lies in the potential applications in many areas of engineering and applied science, which deal with small size systems, including micro- and nanofluidics [2], flow in porous media, friction and lubrication, and biological fluids. The driving and mixing of liquids when the channel size decreases represent a very difficult problem [3]. There is therefore a big hope to cause changes in hydrodynamic behavior by an impact of interfacial phenomena on the flow. For example, even ideal solids, which are both flat and chemically homogeneous, can have a contact angle, which exceeds  $90^\circ$  (the hydrophobic case). This can modify hydrodynamic boundary conditions, as it has been shown yet in early work [4]. Beside that, solids are not ideal, yet rough. This can further change, and quite dramatically, boundary conditions. It is of course interesting and useful to show how the defects or pores of the solids modify them. But today, the question has slightly shifted. Thanks to techniques coming from microelectronics, we are able to elaborate substrates whose surfaces are patterned (often at the micro- and nanometer scale) in a very well controlled way, which provides properties (e.g. optical or electrical) that the solid did not have when flat or slightly disordered. A texture affects the wettability and boundary conditions on a substrate, and can induce unique properties that the material could not have without these micro- and nanostructures. In particular, in case of super-hydrophobic solids, which are generated by a combination of surface chemistry and patterns, roughness can dramatically lower the ability of drops to stick, by leading to the remarkable mobility of liquids. At the macroscopic scale this renders them ‘self-cleaning’ and causes droplets to roll (rather than slide) under gravity and rebound (rather than spread) upon impact instead of spreading [5]. At the smaller scale, reduced wall friction and a superlubricating potential are almost likely associated with the breakdown of the no-slip hypothesis.

In this paper we concentrate on the understanding and expectations for the fluid-solid boundary conditions in different situations, where hydrophobicity and roughness impact the flow properties. After introducing the terminology, and describing new developments and instruments, which give the possibility of investigating fluid behavior at the micro- and nanoscale, in the following section we present results obtained for smooth surfaces, by highlighting the role of wettability. Then follows the results for a rough hydrophilic and, especially, hydrophobic surfaces. In the latter case we show, and

this is perhaps the main message of our paper, how can roughness enhance hydrodynamic slip and thus the efficiency of transport phenomena.

## 2. Terminology

We will refer to as a slip any situation where the value of the tangential component of velocity appears to be different from that of the solid surface. The simplest possible relation assumes that the tangential force per unit area exerted on the solid surface is proportional to the slip velocity. Combining this with the constitutive equation for the bulk Newtonian fluid one gets the so-called (scalar) Navier boundary condition

$$u_s = b \frac{\partial u}{\partial z}, \quad (1)$$

where  $u_s$  is the (tangential) slip velocity at the wall,  $\partial u/\partial z$  the local shear rate, and  $b$  the slip length. This slip length represents a distance inside the solid to which the velocity has to be extrapolated to reach zero. The standard no-slip boundary condition corresponds to  $b = 0$ , and the shear-free boundary condition corresponds to  $b \rightarrow \infty$  [6]. In the most common situation  $b$  is finite (a partial slip) and associated with the positive slip velocity. It can, however, be negative, although in this case it would not have a long-range effect on the flow [7]. Obviously the control of slip lengths is of major importance for flow at interface and in confined geometry. It would be useful to distinguish between three different situations for a boundary slip since the dynamics of fluids at the interface introduce various length scales.

*Molecular* (or intrinsic) slip, which allows liquid molecules to slip directly over solid surface (Fig. 1a). Such a situation is not of main concern here since molecular slip cannot lead to a large  $b$  [4, 8, 9] and its calculations requires a molecular consideration of the interface region. In particular, recent Molecular Dynamics simulations predicted a molecular  $b$  below 10 nm for realistic contact angles [10, 11]. Therefore, it is impossible to benefit of such a slip in a larger scale applications.

The intrinsic boundary condition maybe rather different from what is probed in flow experiment at larger length scale. It has been proposed [6] to describe the interfacial region as a lubricating ‘gas film’ of thickness  $e$  of viscosity  $\eta_g$  different from its bulk value  $\eta$ . A straightforward calculations give *apparent* slip (Fig. 1b)

$$b = e \left( \frac{\eta}{\eta_g} - 1 \right) \simeq e \frac{\eta}{\eta_g} \quad (2)$$

This represents the so-called ‘gas cushion model’ of hydrophobic slippage [6], which got a clear microscopic foundation in terms of a prewetting transition [12]. Being a schematic representation of a depletion close to a wall [13], this model provides a useful insight into the sensitivity of the interfacial transport to the structure of interface. Similarly, electrokinetic flow displays apparent slip.

Another situation is that of *effective* slip,  $b_{\text{eff}}$ , which refers to a situation where slippage at a complex heterogeneous surface is evaluated by averaging of a flow over the length scale of the experimental configuration (e.g. a channel etc) [3, 14, 15, 16].

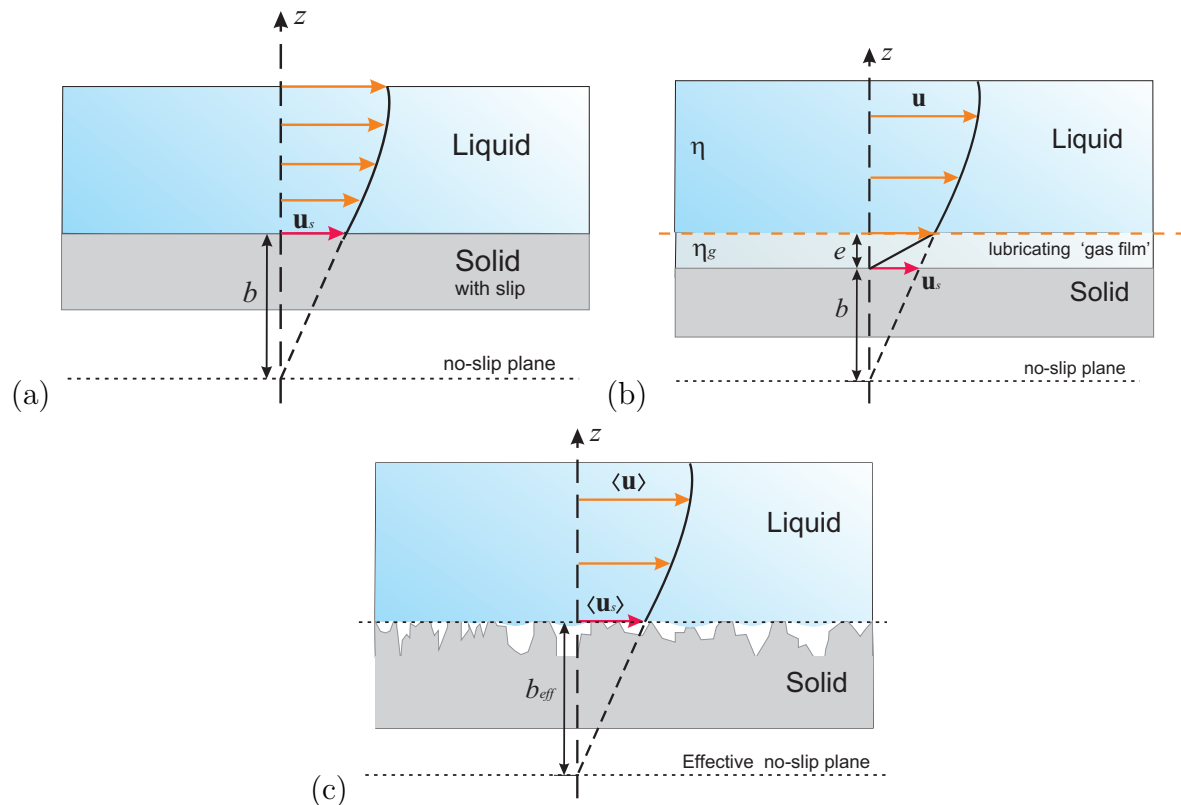


**Figure 1.** Schematic representation of the definition of intrinsic (a), apparent (b), and effective (c) slip lengths.

In other words, rather than trying to solve equations of motion at the scale of the individual corrugation or pattern, it is appropriate to consider the ‘macroscale’ fluid motion (on the scale larger than the pattern characteristic length or the thickness of the channel) by using effective boundary conditions that can be applied at the imaginary smooth surface. Such an effective condition mimics the actual one along the true heterogeneous surface. It fully characterizes the flow at the real surface and can be used to solve complex hydrodynamic problems without tedious calculations. Such an approach is supported by a statistical diffusion arguments (being treated as an example of commonly used Onsager-Casimir relations for non-equilibrium linear response) [14], theory of heterogeneous porous materials [15], and has been justified for the case of Stokes flow over a broad class of surfaces [16]. For anisotropic textures  $b_{\text{eff}}$  depends on the flow direction and is generally a tensor [14]. Effective slip also depends on the interplay between typical length scales of the system as we will see below. Well-known examples of such a heterogeneous system include composite superhydrophobic (Cassie) surfaces, where a gas layer stabilized with a rough wall texture (Fig. 1c). For these surfaces effective slip lengths are often very large compared with the value on flat solids, similarly to what has been observed for wetting, where the contact angle can be dramatically enhanced when surface is rough and heterogeneous [17].

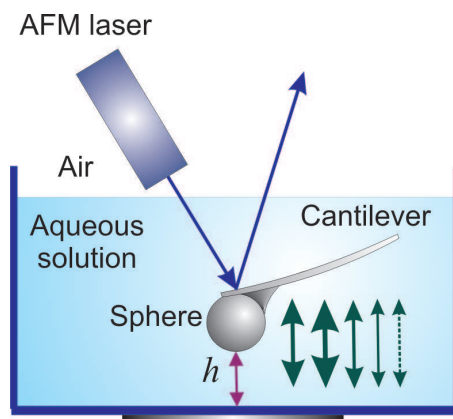


**Figure 2.** Schematic of the dynamic AFM force experiment.

### 3. Experimental methods

The experimental challenge generated a considerable progress in experimental tools for investigating flow boundary conditions, using the most recent developments in optics and scanning probe techniques. A large variability still exists in the results of slip experiments so it is important first to consider the different experimental methods used to measure slip. Two broad classes of experimental approaches have been used so far: indirect and direct (local) methods.

High-speed force measurements can be performed with the SFA (surface forces apparatus) [18, 19, 20] or AFM (atomic force microscope) [21]. In particular, in the drainage method [18, 21] the end of the spring away from the attached sphere is driven toward the (fixed) plane with a constant driving speed (as shown in Fig. 2). The sphere itself, however, does not move at a constant speed, so that the spring is deflected as a result of both the surface force (which should be measured separately) and the hydrodynamic forces. The solution of the (differential) equation of motion allows to deduce a drag force, with the subsequent comparison with a theory of a film drainage [6, 22]. This approach, being extremely accurate at the nanoscale, does not provide visualization of the flow profile, so that these measurements are identified as indirect.

Direct approaches to flow profiling, or velocimetry, take advantage of various optics to monitor tracer particles. These methods include TIR-FRAP (total internal reflection - fluorescence recovery after photo-bleaching) [23],  $\mu$ -PIV [24, 25] (particle image velocimetry), TIRV (total internal reflection velocimetry) [26], EW  $\mu$ -PIV (evanescent wave micro particle image velocimetry) [27], and multilayer nano-particle image velocimetry (nPIV) [28]. Their accuracy is normally much lower than that of force methods due to relatively low optical resolution, system noise due to polydispersity of tracers, and difficulties in decoupling flow from diffusion (the tracer distribution in the flow field is affected by Taylor dispersion [29]). As a consequence, it has been always expected that a slippage of the order of a few tens nanometers cannot be detected

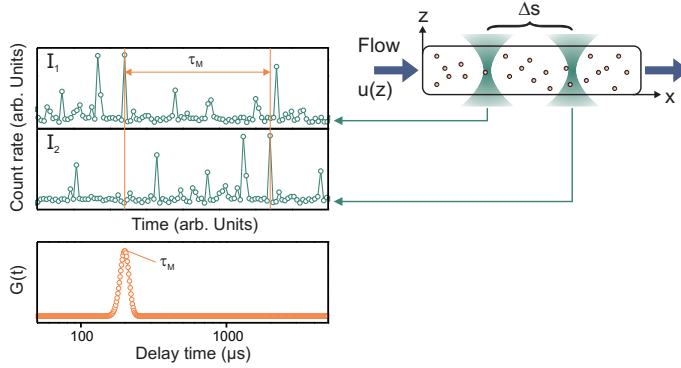


**Figure 3.** Schematics of the double-focus spatial fluorescence cross-correlation method. Two laser foci are placed along the  $x$  axis separated by a distance of a few  $\mu\text{m}$ . They independently record the time-resolved fluorescence intensities  $I_1(t)$  and  $I_2(t)$ . The forward cross-correlation of these two signals yields  $G(t)$ . Two foci are scanned simultaneously along the  $z$  axis to probe the velocity profile  $u(z)$ .

by a velocimetry technique. However, recently direct high-precision measurements at the nanoscale have been performed with a new optical technique, based on a DF-FCS (double-focus spatial fluorescence cross-correlation) [30, 29] (as is schematically shown in Fig. 3). As the fluorescence tracers are flowing along the channel they are crossing consecutively the two foci, producing two time-resolved fluorescence intensities  $I_1(t)$  and  $I_2(t)$  recorded independently. The time cross-correlation function can be calculated and typically exhibits a local maximum. The position of this maximum  $\tau_M$  is characteristic of the local velocity of the tracers. Another example of high resolution applications of FCS consists in determination of average transverse diffusion coefficient to probe slippage [31]. Since FCS methods allow consideration of  $N \sim 10^6$  particles, this gives a satisfactory signal to noise ratio  $\sqrt{N}$  of order  $10^3$ , providing extremely good resolution as compared with other direct velocimetry methods. Coupling with TIRF [32], which allows the measurements of the distance of tracers from the wall through the exponential decay of an evanescent wave, should further improve the accuracy of approach.

Many experiments have been performed on the subject, with somewhat contradicting results. Experimental work focussed mostly on bare (smooth) surface, more recent investigations have turned towards rough and structured surfaces, in particular super-hydrophobic surfaces [33]. We refer the reader to comprehensive review articles [8, 34] for detailed account of early experimental work. Below we mention only what we believe is the most relevant recent contribution to the subject of flow past ‘simple’ smooth surfaces, which clarified the situation, highlighted reasons for existing controversies, and resolved apparent paradoxes. We focus, however, more on the implication of micro- and nanostructuring on fluidic transport, which is still at its infancy and remains to be explored.

#### 4. Smooth surfaces: Slippage vs wetting

From the theoretical [9, 35] and simulation [11, 36] point of view slippage should not appear on a hydrophilic surface, except probably as at very high shear rate [37]. A slip length of the order of hundred nanometers or smaller is, however, expected for a hydrophobic surface [6, 9, 12, 38]. On the experimental side, no consensus was achieved until recently. While some experimental data were consistent with the theoretical expectations both for hydrophilic and hydrophobic surfaces [19, 21], some other reports completely escaped from this picture with both quantitative (slippage over hydrophilic surface, shear rate dependent slippage, rate threshold for slip, etc) and quantitative (slip length of several  $\mu\text{ms}$ ) discrepancies (for a review see [8]). More recent experiments, performed with various new experimental methods, finally concluded that water does not slip on smooth hydrophilic surfaces, and develops a slip only on hydrophobic surface [29, 31, 39, 40, 41, 42]. One can therefore conclude that a concept of hydrophobic slippage is now widely accepted.

An important issue is the amplitude of hydrophobic slip. The observed slip length reached the range 20-100 nm, which is above predictions of the models of molecular slip [10, 43]. This suggests the apparent slip, such as the ‘gas cushion model’, Eq. (2). Water glides on air, owing to the large viscosity ratio between water and air (typically a factor of 50). Experimental values of  $b$  suggest that the thickness of this ‘layer’ is below 2 nm. A modification of this scenario would be a nanobubble coated surface [44, 45, 46, 47]. Another important conclusion is that it is impossible to benefit of such a nanometric slip at separations  $O(\mu\text{m})$  and larger, i.e. in microfluidic applications. This is why in the discussion of super-hydrophobic slippage below we often ignore a slip past hydrophobic solids. However, a hydrophobic slippage is likely of major importance in nanochannels (highly confined hydrophobic pores, biochannels, etc), where ordinary Poiseuille flow is fully suppressed.

#### 5. Rough surfaces

Only a very few solids are molecularly smooth. Most of them are naturally rough, often at a micro- and nanoscale, due to their structure, methods of preparation, various coatings. These surfaces are very often in the Wenzel (impaled) state, where solid/liquid interface has the same area as the solid surface (Fig. 4a). However, even for rough hydrophilic Wenzel surfaces the situation was not very clear, and opposite experimental conclusions have been made: one is that roughness generates extremely large slip [48], and one is that it decreases the degree of slippage [49, 50]. More recent experimental data suggests that the description of flow near rough surfaces has to be corrected, but for a separation, not slip [39]. The theoretical description of such a flow represents a difficult, nearly insurmountable, problem. It has been solved only approximately, and only for a case of the periodic roughness and far-field flow with a conclusion that it may be possible to approximate the actual surface by a smooth one with the slip boundary

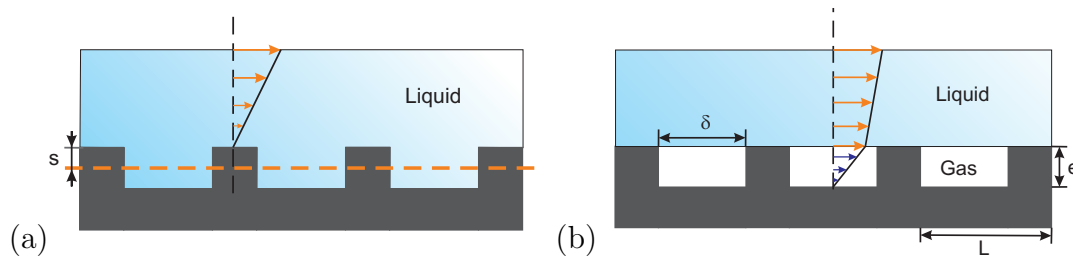


**Figure 4.** Schematic representation of the (a) Wenzel and (b) Cassie pictures with the local flow profiles at the gas and solid areas.

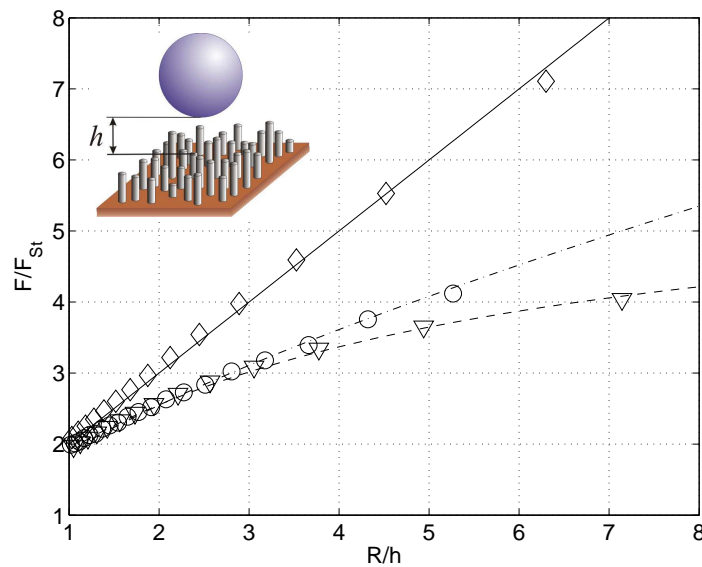


**Figure 5.** Hydrodynamic force acting on a hydrophilic sphere of radius  $R$  approaching a smooth hydrophilic (diamonds), smooth hydrophobic (circles) and randomly rough hydrophilic (triangles) wall with  $\phi_2 = 4\%$  (adapted from [36]). Here  $F_{St} = 6\pi\eta RU$  is the Stokes drag. The separation  $h$  is defined on top of the surface roughness as shown in the inset. Simulation results (symbols) compared with theoretical curves:  $F/F_{St} = 1 + 9R/(8h)$  (solid),  $F/F_{St} = 1 + 9Rf^*/(8h)$  with  $f^* = f(b/h)$  taken from [7] (dash-dotted), and  $F/F_{St} = 1 + 9R/(8[h + s])$  (dashed). Values of  $b$  and  $s$  were determined by fitting the simulation data.

condition [51, 52, 53].

This issue was recently resolved in the LB (lattice Boltzmann) simulation study [36] where the hydrodynamic interaction between a smooth sphere of radius  $R$  and a randomly rough plane was studied (as shown in Fig. 5). Beside its significance as a geometry of SFA/AFM dynamic force experiments, this allowed one to explore both far and near-field flows in a single ‘experiment’. The ‘measured’ hydrodynamic force was smaller than predicted for two smooth surfaces (with the separation defined at the top of asperities) if the standard no-slip boundary conditions are used in the calculation. Moreover, at small separations the force was even weaker and shows



different asymptotics than expected if one invokes slippage at the smooth fluid-solid interfaces. This can only be explained by the model of a no-slip wall, located at an intermediate position (controlled by the density of roughness elements) between top and bottom of asperities (illustrated by dashed line Fig. 4a). Calculations based on this model provided an excellent description of the simulation data (Fig. 5).

## 6. Super-hydrophobicity and effective hydrodynamic slippage

On hydrophobic solids, the situation is different from that on hydrophilic solids. If the solid is rough enough, we do not expect that the liquid will conform to the solid surface, as assumed in the Wenzel or impaled state. Rather air pockets should form below the liquid, provided that the energetic cost associated with all the corresponding liquid/vapor interfaces is smaller than the energy gained not to follow the solid [5]. This is so-called Cassie or fakir state. Hydrophobic Cassie materials generate large contact angles and small hysteresis, ideal conditions for making water drops very mobile. It is natural to expect a large effective slip in a Cassie situation. Indeed, taking into account that the variation of the texture height,  $e$ , is in the typical interval  $0.1 - 10 \mu\text{m}$ , according to Eq.(2) we get  $b = 5 - 500 \mu\text{m}$  at the gas area. The composite nature of the texture requires regions of very low slip (or no slip) in direct contact with the liquid, so the effective slip length of the surface,  $b_{\text{eff}}$ , is smaller than  $b$ . Still, one can expect that a rational design of such a texture could lead to a large values of  $b_{\text{eff}}$ . Below we make these arguments more quantitative.

We will examine an idealized super-hydrophobic surface in the Cassie state sketched in Fig. 4b where a liquid slab lies on top of the surface roughness. The liquid/gas interface is assumed to be flat with no meniscus curvature, so that the modeled super-hydrophobic surface appears as a perfectly smooth with a pattern of boundary conditions. In the simplified description the latter are taken as no-slip ( $b_1 = 0$ ) over solid/liquid areas and as partial slip ( $b_2 = b$ ) over gas/liquid regions [as we have shown above,  $b_1$  is of the orders of tens nm, so that we could neglect it since  $b_2$  is of the order of tens of  $\mu\text{m}$ ]. We denote as  $\delta$  a the typical length scale of gas/liquid areas. The fraction of solid/liquid areas will be denoted  $\phi_1 = (L - \delta)/L$ , and of gas/liquid area  $\phi_2 = 1 - \phi_1 = \delta/L$ . Overall, the description of a super-hydrophobic surface we use is similar to those considered in Refs [15, 54, 55, 56, 57]. In this idealization, some assumptions may have a possible influence on the friction properties and, therefore, a hydrodynamic force. First, by assuming flat interface, we have neglected an additional mechanism for a dissipation connected with the meniscus curvature [58, 59, 60]. Second, we ignore a possible transition towards impaled (Wenzel) state that can be provoked by additional pressure in the liquid phase [61, 62].

Finally, for the sake of brevity we focus below only on the canonical microfluidic geometry where the fluid is confined between flat plates, and only on the asymmetric case, where one (upper) surface is smooth hydrophilic and another (lower) represents a super-hydrophobic wall in the Cassie state. Such a configuration is relevant for various

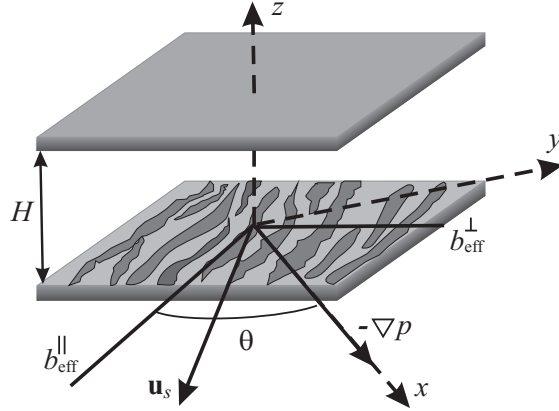


**Figure 6.** Sketch of a flat channel of thickness  $H$  wall with notation for directions along the plates. One wall represents an anisotropic super-hydrophobic texture.

setups, where the alignment of opposite textures is inconvenient or difficult. We also restrict the discussion by a pressure-driven flow governed by the Stokes equations:

$$\eta \nabla^2 \mathbf{u} = \nabla p, \quad \nabla \cdot \mathbf{u} = 0, \quad (3)$$

where  $\mathbf{u}$  is the velocity vector, and  $p$  is pressure. Extensions of our analysis to study other configuration geometries and types of flow would be straightforward.

### 6.1. Anisotropic surfaces.

Many natural and synthetic textures are isotropic. However, it can be interesting to design directional structures, such as arrays of parallel grooves or microwrinkles, that consequently generate anisotropic effective slip in the Cassie regime. The hydrodynamic slippage is quite different along and perpendicular to the grooves. Axial motion is preferred, and such designs are appropriate when liquid must be guided. There are examples of such patterns in nature, such as the wings of butterflies or water striders.

The flow past such surfaces becomes misaligned with the pressure gradient, which has been analyzed in a number of studies [63, 64]. Such phenomena have motivated a tensorial version of (1), as discussed in [3, 14]

$$\langle u_i |_A \rangle = \sum_{j,k} b_{ij}^{\text{eff}} n_k \left\langle \frac{\partial u_j}{\partial x_k} \Big|_A \right\rangle, \quad (4)$$

where  $\langle \mathbf{u} |_A \rangle$  is the effective slip velocity, averaged over the surface pattern and  $\mathbf{n}$  is a unit vector normal to the surface  $A$ . The second-rank effective slip tensor  $\mathbf{b}_{\text{eff}} \equiv \{b_{ij}^{\text{eff}}\}$  characterizes the surface anisotropy and is represented by symmetric, positive definite  $2 \times 2$  matrix diagonalized by a rotation:

$$\mathbf{b}_{\text{eff}} = \mathbf{S}_\theta \begin{pmatrix} b_{\text{eff}}^{\parallel} & 0 \\ 0 & b_{\text{eff}}^{\perp} \end{pmatrix} \mathbf{S}_{-\theta}, \quad \mathbf{S}_\theta = \begin{pmatrix} \cos \theta & \sin \theta \\ -\sin \theta & \cos \theta \end{pmatrix}. \quad (5)$$

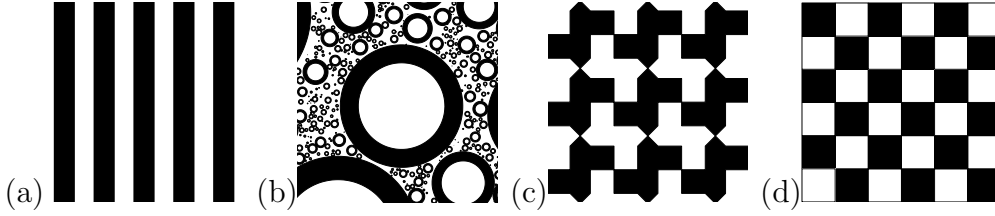


**Figure 7.** Special textures arising in the theory: (a) stripes, which attain the Wiener bounds of maximal and minimal effective slip, if oriented parallel or perpendicular to the pressure gradient, respectively; (b) the Hashin-Shtrikman fractal pattern of nested circles, which attains the maximal/minimal slip among all isotropic textures (patched should fill up the whole space, but their number is limited here for clarity); and (c) the Schulgasser and (d) chessboard textures, whose effective slip follows from the phase-interchange theorem.

As proven in [14] for all anisotropic surfaces the eigenvalues  $b_{\text{eff}}^{\parallel}$  and  $b_{\text{eff}}^{\perp}$  of the slip-length tensor correspond to the fastest (greatest forward slip) and slowest (least forward slip) directions, which are always orthogonal (see Fig. 6).

To illustrate the calculation of the slip-length tensor, below we consider the geometry where the liquid is confined between two plates separated by a distance  $H$ , and one of them represents a super-hydrophobic striped wall (Fig. 7a).

*6.1.1. General solution* We calculate the effective slip lengths in eigendirections (which are in this case obviously parallel and orthogonal to stripes), by solving Stokes equations, Eqs.(3). The  $x$ -axis is directed along the pressure gradient  $\langle \nabla p \rangle = (-\sigma, 0, 0)$ . Essentially, since along these orthogonal directions there are no transverse hydrodynamic couplings [14], the pressure gradient  $\langle \nabla p \rangle$  coincides with the direction of slip for longitudinal and transverse stripes. We seek the solution for a velocity  $\mathbf{u}$  by using the perturbation analysis:

$$\mathbf{u} = \mathbf{u}_0 + \mathbf{u}_1, \quad (6)$$

where  $\mathbf{u}_0$  is the velocity of the Poiseuille flow, and the effective slip length  $b_{\text{eff}}$  at the super-hydrophobic surface is defined as:

$$b_{\text{eff}} = \frac{\langle u_{z=0} \rangle}{\langle \left( \frac{\partial u}{\partial z} \right)_{z=0} \rangle}, \quad (7)$$

where  $u$  denotes  $x$ -component of the velocity and  $\langle \dots \rangle$  means the average value in plane  $xOy$ .

The effective slip length can now be calculated by using the dual series technique suggested in recent work [60, 55]. By employing a family of Fourier series solutions to Eqs.(3) together with boundary conditions

$$\mathbf{u}(x, y, 0) = b(x, y) \cdot \frac{\partial \mathbf{u}}{\partial z}(x, y, 0), \quad \hat{\mathbf{z}} \cdot \mathbf{u}(x, y, 0) = 0. \quad (8)$$

$$\mathbf{u}(x, y, H) = 0, \quad \hat{\mathbf{z}} \cdot \mathbf{u}(x, y, H) = 0, \quad (9)$$

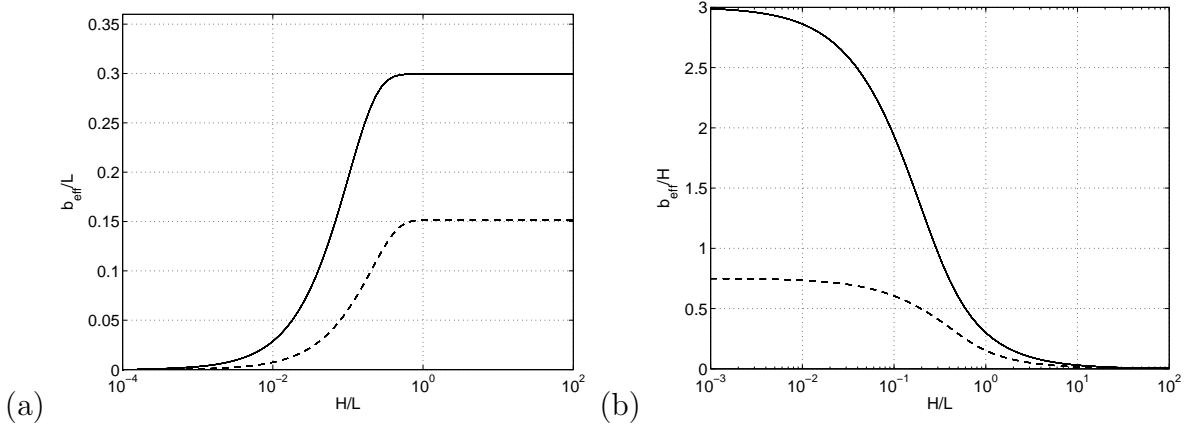


**Figure 8.** Eigenvalues  $b_{\text{eff}}^{\parallel}$  (solid curve) and  $b_{\text{eff}}^{\perp}$  (dashed curve) of the slip length tensor for stick-slip stripes of period  $L$  with local slip length at liquid-gas interface  $b/L = 20$  and slipping area fraction  $\phi_2 = 0.75$  as a function of the thickness of the channel,  $H$ .

we obtain the dual series problem (in dimensionless form) for longitudinal and transverse configurations

$$\alpha_0 \left(1 + \frac{\beta}{h}\right) + \sum_{n=1}^{\infty} \alpha_n [1 + \beta n V(nh)] \cos(n\xi) = \beta, \quad 0 < \xi \leq \pi\phi_2, \quad (10)$$

$$\alpha_0 + \sum_{n=1}^{\infty} \alpha_n \cos(n\xi) = 0, \quad \pi\phi_2 < \xi \leq \pi, \quad (11)$$

where  $\{\xi, h, \beta\} = (2\pi/L) \cdot \{z, H, b\}$ , and the function  $V(x)$  is defined as:

$$V(x) = \coth(x) \quad (12)$$

for a longitudinal flow, and

$$V(x) = 2 \frac{\sinh(2x) - 2x}{\cosh(2x) - 2x^2 - 1} \quad (13)$$

for a transverse flow. The effective slip length is then

$$b_{\text{eff}} = \frac{L}{2\pi} \frac{\alpha_0}{1 - \alpha_0/h}. \quad (14)$$

Following [60] we can now use the orthogonality of trigonometric sine and cosine functions to obtain the system of linear algebraic equations:

$$\sum_{n=0}^{\infty} A_{nm} \alpha_n = B_m, \quad (15)$$

which can be solved in respect to  $\alpha_n$ . Fig. 8a shows the typical calculation results (the numerical example corresponds to  $b/L = 20$  and  $\phi_2 = 0.75$ ), and demonstrates that the effective slip lengths increase with  $H$  and saturate for a thick gap. This points to the fact that an effective boundary condition *is not* a characteristic of liquid/solid interface solely, but depends on the flow configuration and interplay between typical length scales,  $L$ ,  $H$ , and  $b$ , of the problem. Next we discuss asymptotic limits (of small and large gaps) of our semi-analytical solution.

6.1.2. *Thin channel* Taylor expansion of  $V(x)$  in the vicinity of  $x = 0$

$$\coth x|_{x \rightarrow 0} = x^{-1} + O(x), \quad (16)$$

$$2 \frac{\sinh(2x) - 2x}{\cosh(2x) - 2x^2 - 1} |_{x \rightarrow 0} = 4x^{-1} + O(x), \quad (17)$$

allows us to find analytical expressions for  $\alpha_0$  and  $b_{\text{eff}}$  in limit of  $H \ll L$ . By substituting them into (10) and (11), we get

$$b_{\text{eff}}^{\parallel} \simeq \frac{bH\phi_2}{H + b\phi_1}, \quad b_{\text{eff}}^{\perp} \simeq \frac{bH\phi_2}{H + 4b\phi_1}. \quad (18)$$

These expressions are independent on  $L$ , but depend on  $H$ , and suggest to distinguish between two separate cases.

If  $b \ll H$  we obtain

$$b_{\text{eff}}^{\perp} \simeq b_{\text{eff}}^{\parallel} \simeq b\phi_2, \quad (19)$$

so that despite the surface anisotropy we predict a simple surface averaged effective slip. Although this limit is less important for pressure-driven microfluidics, it may have relevance for amplifying transport phenomena [65].

When  $H \ll b$  we derive

$$b_{\text{eff}}^{\parallel} \simeq H \frac{\phi_1}{\phi_2}, \quad b_{\text{eff}}^{\perp} \simeq \frac{1}{4} b_{\text{eff}}^{\parallel}. \quad (20)$$

The above formula implies the effective slip length is generally four times as large for parallel versus perpendicular pressure driven flow. Both asymptotic results, Eqs.(19) and (20), are surprising taking into account that for anisotropic Stokes flow in a thick channel factor of two is often expected as reminiscent results for striped pipes [66], sinusoidal grooves [16] and the classical result that a rod sediments twice as fast in creeping flow if aligned vertically rather than horizontally [67]. A very important conclusion from our analysis is that this standard scenario can significantly differ in a thin super-hydrophobic channel, by giving a whole spectrum of possibilities, from isotropic to highly anisotropic flow, depending on the ratio  $b/H$ .

Note that in case of a thin channel the flow can be described by an expression of Darcy's law, which relates the depth-averaged fluid velocity to an average pressure gradient along the plates through the effective permeability of the channel. The permeability,  $\mathbf{K}_{\text{eff}}$ , is in turn expressed through effective slip length  $\mathbf{b}_{\text{eff}}$ , and permeability and slip-length tensors are coaxial. Such an approach allows one to use the theory of transport in heterogeneous media [68], which provides *exact* results for an effective permeability over length scales much larger than the heterogeneity. This theory allows one to derive rigorous bounds on an effective slip length for arbitrary textures, given only the area fraction and local (any) slip lengths of the low-slip ( $b_1$ ) and high-slip ( $b_2$ ) regions [15, 69]. These bounds constrain the attainable effective slip and provide theoretical guidance for texture optimization, since they are attained only by certain special textures in the theory. In some regimes, the bounds are close enough to obviate the need for tedious calculations of flows over particular textures. In particular, by

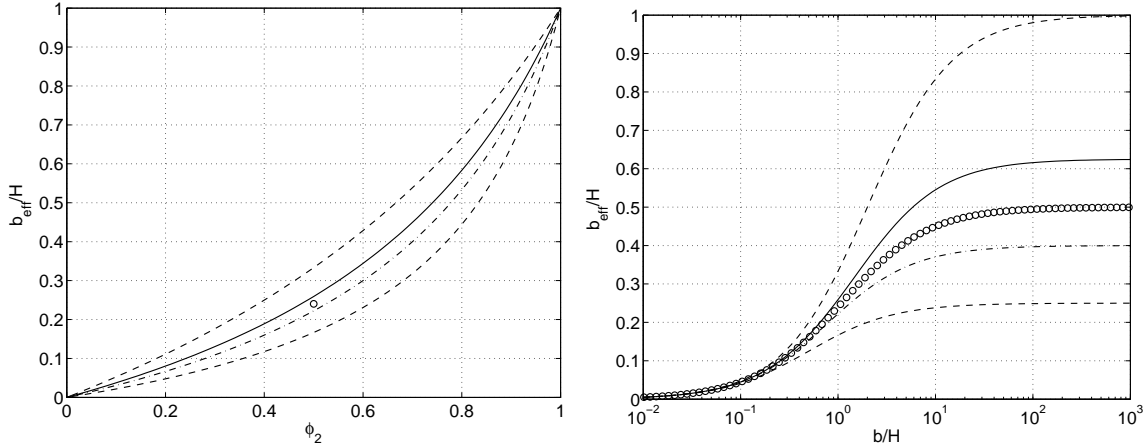


**Figure 9.** Effective slip length,  $b_{\text{eff}}/H$ , versus  $\phi_2$  [for  $b/H = 1$ ] (left) and  $b/H$  [for  $\phi_2 = 0.5$ ] (right) in a thin gap limit,  $H \ll L$ . SH surfaces are: anisotropic stick-slip stripes attaining Wiener bounds (dashed curves), isotropic textures attaining Hashin-Shtrickman bounds (upper – solid, lower – dash-dotted curves) and satisfying the phase-interchange theorem (circles).

using the general result of the theory of bounds [15] one can easily derive Eq.(18) and its limits, as well as to prove that for a thin channel longitudinal (transverse) stripes satisfy upper (lower) Wiener bounds, i.e. provide the largest (smallest) possible slip that can be achieved by any texture. We remark and stress that according to results [15] stripes should not be necessarily periodic.

Typical dependence of Wiener bounds for  $b_{\text{eff}}/H$  on  $\phi_2$  (at fixed  $b/H$ ) and on  $b/H$  (at fixed  $\phi_2$ ) is shown in Fig. 9, which well illustrates that the key parameters determining effective slip in the thin channel is the area fraction of solid,  $\phi_1$ , in contact with the liquid. If this is very small (or  $\phi_2 \rightarrow 1$ ), for all textures the effective slip tends to a maximum value,  $b_{\text{eff}} \rightarrow b$ . We can also conclude that maximizing  $b$  also plays a important role to achieve large effective slip.

*6.1.3. Thick channel* In the opposite case of infinitely large thickness ( $H \gg L$ ) the dual series problems Eqs.(10),(11) reduce to those studied in recent work [55], due to  $V(x \rightarrow \infty) \rightarrow 1$  and 2 for longitudinal and transverse stripes respectively. Thus, the effective slip lengths in this case [55]

$$b_{\text{eff}}^{\parallel} \simeq \frac{L}{\pi} \frac{\ln \left[ \sec \left( \frac{\pi \phi_2}{2} \right) \right]}{1 + \frac{L}{\pi b} \ln \left[ \sec \left( \frac{\pi \phi_2}{2} \right) + \tan \left( \frac{\pi \phi_2}{2} \right) \right]}, \quad (21)$$

$$b_{\text{eff}}^{\perp} \simeq \frac{L}{2\pi} \frac{\ln \left[ \sec \left( \frac{\pi \phi_2}{2} \right) \right]}{1 + \frac{L}{2\pi b} \ln \left[ \sec \left( \frac{\pi \phi_2}{2} \right) + \tan \left( \frac{\pi \phi_2}{2} \right) \right]}. \quad (22)$$

The above results apply for a single surface, and are independent on  $H$ . However, these expressions for effective slip lengths depend strongly on a texture period  $L$ . When  $b \ll L$  we again derive the area-averaged slip length, Eq.(19). When  $b \gg L$ , expressions (21) and (22) take form

$$b_{\text{eff}}^{\perp} \simeq \frac{L}{2\pi} \ln \left[ \sec \left( \frac{\pi\phi_2}{2} \right) \right], \quad b_{\text{eff}}^{\parallel} \simeq 2b_{\text{eff}}^{\perp}, \quad (23)$$

that coincides with the result obtained by Lauga and Stone [66] for the ideal slip ( $b \rightarrow \infty$ ) case. We stress that the commonly expected factor of two for the ratio of  $b_{\text{eff}}^{\parallel}$  and  $b_{\text{eff}}^{\perp}$  is predicted only for very large  $b/L$ . In all other situation the anisotropy of the flow is smaller and even disappears at moderate  $b/L$ .

## 6.2. Isotropic surfaces.

As stressed above most solids are isotropic, i.e. without a preferred direction. Unfortunately, from the hydrodynamic point of view, this situation is more complicated than considered above. Below we discuss only some aspects of the hydrodynamic behavior in the thin and thick channel situations. For a thin channel, our arguments are based on the already mentioned theory of transport in heterogeneous media [68] and derived bounds on an effective slip length (effective slip length and permeability tensors are now becoming simply proportional to the unit tensor  $\mathbf{I}$ ) for arbitrary isotropic textures [15, 69]. For a thick channel, the only available arguments are based on the scaling theory and numerical calculations [54], which however provide us with some guidance.

*6.2.1. Thin channel* If the only knowledge about the two-phase isotropic texture is  $\phi_1, \phi_2$ , then the Hashin-Shtrikman (HS) bounds apply for the effective permeability, by giving the corresponding upper and lower HS bounds for the effective slip length [15, 69]. These bounds can be attained by the special HS fractal pattern sketched in Fig. 7b. For one bound, space is filled by disks of all sizes, each containing a circular core of one component and a thick ring of the other (with proportions set by the concentration), and switching the components gives the other bound. Fractal geometry is not necessary, however, since periodic honeycomb-like structures can also attain the bounds. The general solution [15, 69] allows to deduce a consequential analytical results for an asymmetric case considered in this paper. The upper (HS) bound can be then presented as

$$b_{\text{eff}} = \frac{bH\phi_2(2H + 5b)}{H(2H + 5b) + b\phi_1(5H + b)}, \quad (24)$$

and the lower (HS) bound reads

$$b_{\text{eff}} = \frac{2bH\phi_2}{2H + 5b\phi_1}. \quad (25)$$

At small  $b/H$  we get Eq.(19), and at large  $b/H$  these give for upper and lower bounds

$$b_{\text{eff}} = \frac{5H\phi_2}{8\phi_1}, \quad \text{and} \quad b_{\text{eff}} = \frac{2H\phi_2}{5\phi_1}, \quad (26)$$

correspondingly.

Finally, phase interchange results [15] can be applied for some specific patterns (Fig. 7c,d). The phase interchange theorem states that the effective permeability  $\mathbf{K}_{\text{eff}}(b_1, b_2)$  of the medium, when rotated by  $\pi/2$ , is related to the effective permeability of the medium obtained by interchanging phases 1 and 2, viz.  $\mathbf{K}_{\text{eff}}(b_2, b_1)$ :

$$[\mathbf{R} \cdot \mathbf{K}_{\text{eff}}(b_1, b_2) \cdot \mathbf{R}^t] \cdot \mathbf{K}_{\text{eff}}(b_2, b_1) = K_1 K_2 \mathbf{I}$$

where  $b_{1,2}$  are the local slip lengths for each medium,  $\mathbf{R}$  is the rotation tensor and  $\mathbf{R}^t$  is its transpose. In the particular case of a medium which is invariant by a  $\pi/2$  rotation followed by a phase interchange, the classical result follows:

$$K_{\text{eff}} = \sqrt{K_1 K_2}$$

Obviously,  $\phi_1 = \phi_2 = 0.5$  for such a medium so that:

$$b_{\text{eff}} = \frac{3H}{4 - \sqrt{1 + \frac{3b}{H+b}}} - H, \quad (27)$$

At  $b/H \ll 1$  we again derive Eq.(19), indicating that at this limit all textures show a kind of universal behavior and the effective slip coincides with the average. This suggests that the effective slip is controlled by the smallest scale of the problem [9, 55], so that at this limit  $b_{\text{eff}}$  is no longer dependent on  $H$ , being proportional to  $b$  only. If  $b/H \gg 1$  we simply get

$$b_{\text{eff}} = \frac{H}{2} \quad (28)$$

again suggesting a kind of universality, i.e. similarly to anisotropic stripes (cf. Eq. 20), in this limit  $b_{\text{eff}}/H$  for all isotropic textures almost likely scale as  $\propto \phi_2/\phi_1$ .

The results for these special textures are included in Fig. 9, which shows that Hashin-Strickman bounds are relatively close and confined between Wiener ones. For completeness, we give in Table 1 a summary of main expressions for an effective slip in a thin channel.

*6.2.2. Thick channel* For this situation the exact solution was not found so far. Nevertheless, some simple scaling expressions have been proposed for a geometry of pillars [9, 54], by predicting  $b_{\text{eff}} \propto L/(\pi\sqrt{\phi_1})$  (cf. scaling results for stripes  $b_{\text{eff}} \propto L/\ln(1/\phi_1)$ ). This simple result would deserve some analytical justification, which has not been performed up to now.



**Table 1.** The effective slip length  $b_{\text{eff}}$  for different textures (shown in Fig. 7) in a thin gap limit ( $H \ll L$ )

Texture	$b_{\text{eff}}$
Wiener upper bound (longitudinal stripes)	$\frac{bH\phi_2}{H + b\phi_1}$
Wiener lower bound (transverse stripes)	$\frac{bH\phi_2}{H + 4b\phi_1}$
Hashin-Shtrickman upper bound (Hashin-Shtrickman fractal, honeycomb-like texture)	$\frac{bH\phi_2(2H + 5b)}{H(2H + 5b) + b\phi_1(5H + b)}$
Hashin-Shtrickman lower bound (Hashin-Shtrickman fractal, honeycomb-like texture)	$\frac{2bH\phi_2}{2H + 5b\phi_1}$
Phase interchange patterns (Schulgasser texture, family of chessboards)	$\frac{3H}{4 - \sqrt{1 + 3b/(H + b)}} - H$

## 7. Other special properties of super-hydrophobic surfaces

As we see above, hydrophobic Cassie materials generate large and anisotropic effective slippage compared to simple, smooth channels, ideal situation for various potential applications. A straightforward implication of super-hydrophobic slip would be the great reduction of the viscous drag of thin microchannels (enhanced *forward* flow), and some useful examples can be found in [14]. Below we illustrate the potential of super-hydrophobic surfaces and possibilities of the effective slip approach by discussing a couple of other applications. Namely, we show that optimized super-hydrophobic textures may be successfully used in a passive microfluidic mixing and for a reduction of a hydrodynamic drag force.

### 7.1. Transverse flow

The effective hydrodynamic slip [3, 14, 16] of anisotropic textured surfaces is generally tensorial, which is due to secondary flows *transverse* to the direction of the applied pressure gradient. In the case of grooved no-slip surfaces (Wenzel state), such a flow has been analyzed for small height variations [70] and thick channels [71], and herringbone patterns have been designed to achieve passive chaotic mixing during pressure-driven

flow through a microchannel [64, 72]. In principle, similar effects may be generated by a super-hydrophobic Cassie surface. To explore this possibility and to illustrate the use of slip tensors we consider now a velocity field in a channel with the focus on a transverse flow optimization, which is necessary for mixing in a microfluidic channel.

By solving Stokes equations, Eq.(3), for a geometry of super-hydrophobic stripes with the *effective* boundary condition at  $z = 0$ :

$$\begin{pmatrix} \langle u_x \rangle \\ \langle u_y \rangle \end{pmatrix} = \begin{pmatrix} b_{\text{eff}}^{\parallel} \cos^2 \theta + b_{\text{eff}}^{\perp} \sin^2 \theta & (b_{\text{eff}}^{\parallel} - b_{\text{eff}}^{\perp}) \sin \theta \cos \theta \\ (b_{\text{eff}}^{\parallel} - b_{\text{eff}}^{\perp}) \sin \theta \cos \theta & b_{\text{eff}}^{\parallel} \sin^2 \theta + b_{\text{eff}}^{\perp} \cos^2 \theta \end{pmatrix} \cdot \begin{pmatrix} \langle \partial_z u_x \rangle \\ \langle \partial_z u_y \rangle \end{pmatrix}$$

we obtain components of the effective velocity

$$\langle u_x \rangle = -\frac{\sigma z^2}{2\eta} + \frac{\sigma H z}{2\eta} + C_x \left(1 - \frac{z}{H}\right), \quad \langle u_y \rangle = C_y \left(1 - \frac{z}{H}\right) \quad (29)$$

with

$$C_x = \frac{\sigma H^2}{2\eta} \frac{H b_{\text{eff}}^{\parallel} \cos^2 \theta + H b_{\text{eff}}^{\perp} \sin^2 \theta + b_{\text{eff}}^{\parallel} b_{\text{eff}}^{\perp}}{(H + b_{\text{eff}}^{\parallel})(H + b_{\text{eff}}^{\perp})},$$

$$C_y = \frac{\sigma H^3}{2\eta} \frac{(b_{\text{eff}}^{\parallel} - b_{\text{eff}}^{\perp}) \sin \theta \cos \theta}{(H + b_{\text{eff}}^{\parallel})(H + b_{\text{eff}}^{\perp})},$$

Note that our results show that the effective velocity profile is ‘twisted’ close to the super-hydrophobic wall (see Fig. 10a). In other words, the transverse flow due to surface anisotropy is generated only in the vicinity of the wall and disappears far from it, which has already been observed in experiment [73].

To evaluate the transverse flow we first integrate the velocity profile across the channel to obtain the flow vector:

$$\mathbf{Q} = \int_0^H \langle \mathbf{u}(z) \rangle dz \quad (30)$$

with the components (according to (29)):

$$Q_x = \frac{\sigma H^3}{\eta 12} \left[ 1 + 3 \frac{(H b_{\text{eff}}^{\parallel} \cos^2 \theta + H b_{\text{eff}}^{\perp} \sin^2 \theta + b_{\text{eff}}^{\parallel} b_{\text{eff}}^{\perp})}{(H + b_{\text{eff}}^{\parallel})(H + b_{\text{eff}}^{\perp})} \right], \quad (31)$$

$$Q_y = \frac{\sigma H^4}{\eta 4} \frac{(b_{\text{eff}}^{\parallel} - b_{\text{eff}}^{\perp}) \sin \theta \cos \theta}{(H + b_{\text{eff}}^{\parallel})(H + b_{\text{eff}}^{\perp})}. \quad (32)$$

Next we consider the fraction  $|Q_y/Q_x|$ . Our aim is to optimize the texture, channel thickness and the angle  $\theta$  between the directions of stripes and the pressure gradient, so that  $|Q_y/Q_x|$  is maximum providing the best transverse flow.

The maximization in respect to  $\theta$  indicates that the optimal angle is

$$\theta_{\text{max}} = \pm \arctan \left[ \frac{(1 + 4b_{\text{eff}}^{\parallel}/H)(1 + b_{\text{eff}}^{\perp}/H)}{(1 + b_{\text{eff}}^{\parallel}/H)(1 + 4b_{\text{eff}}^{\perp}/H)} \right]^{1/2}. \quad (33)$$

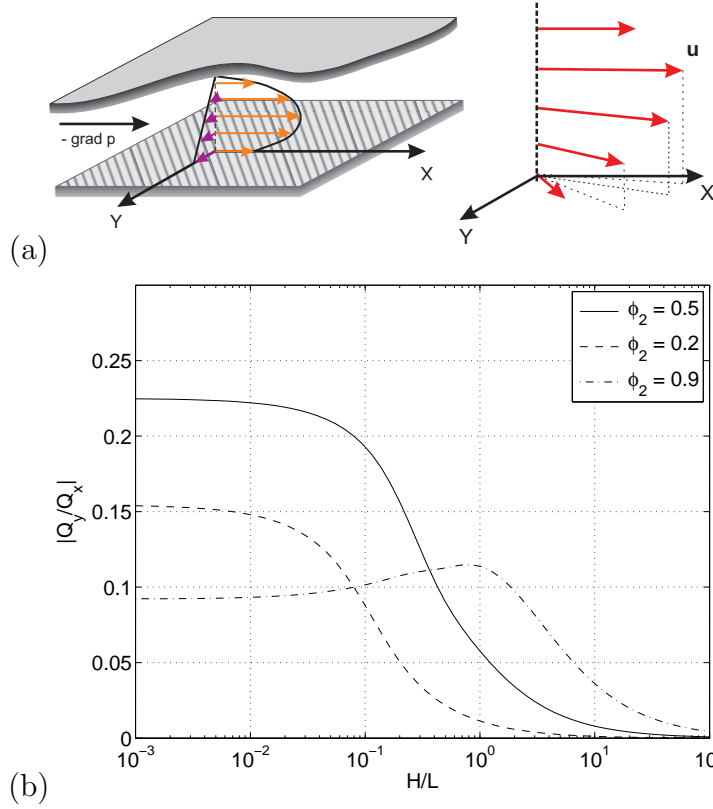


**Figure 10.** (a) Scheme of a transverse flow generation. (b) Fraction of flow vector  $\mathbf{Q}$  components (maximized over  $\theta$ ) as function of channel thickness for local slip  $b/L = 1000$  and slip fraction  $\phi_2 = 0.5$  (solid line), 0.2 (dashed) and 0.9 (dash-dot).

The value of the maximum is

$$\left| \frac{Q_y}{Q_x} \right| = \frac{1}{2} \left( \tan \theta_{\max} - \frac{1}{\tan \theta_{\max}} \right). \quad (34)$$

We conclude, therefore, that since  $H$  is fixed, the maximal  $|Q_y/Q_x|$  corresponds to the largest physically possible  $b$ , i.e. the perfect slip at the gas sectors.

To optimize the fraction of the slipping area,  $\phi_2$ , we should now exploit results for effective slip lengths  $b_{\text{eff}}^{\parallel, \perp}$  obtained above. Fig.10b shows the computed value of  $|Q_y/Q_x|$  vs.  $H/L$  for several  $\phi_2$ . The calculations are made using the value of  $\theta$  defined by Eq.(33). The data suggest that the effect of  $\phi_2$  on a transverse flow depends on the thickness of the channel. For a thick gap the increase in gas fraction,  $\phi_2$ , augments a transverse flow. This result has a simple explanation. For an infinite channel  $b_{\text{eff}}^{\parallel, \perp}/H \ll 1$  (see Fig.(9b)), which gives

$$\left| \frac{Q_y}{Q_x} \right|_{H \rightarrow \infty} \simeq \frac{3}{2} \frac{\Delta b_{\text{eff}}}{H}, \quad (35)$$

i.e. in a thick channel the amplitude of a transverse flow is controlled by the difference between eigenvalues of the effective slip tensor,  $\Delta b_{\text{eff}} = b_{\text{eff}}^{\parallel} - b_{\text{eff}}^{\perp}$ , which increases with  $\phi_2$  as follows from the above analysis. We stress however, that since  $|Q_y/Q_x| \propto H^{-1}$ ,

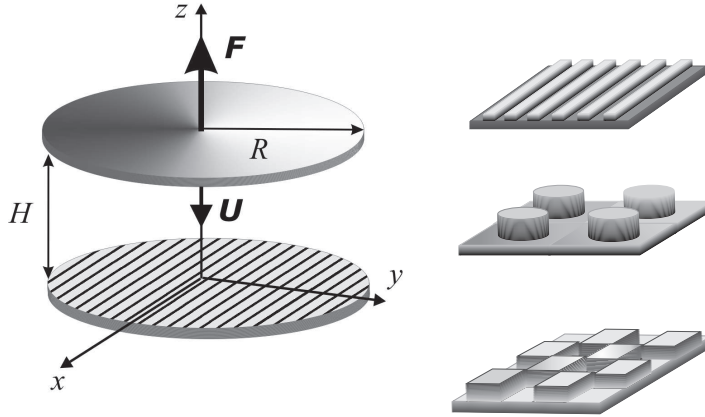


**Figure 11.** (Left) Sketch of a hydrophilic disk approaching super-hydrophobic striped disk. (Right) Example of anisotropic (grooves) and isotropic (pillars, chess-board) textures.

the mixing in a thick super-hydrophobic channel would be not very efficient. A more appropriate situation corresponds to a thin channel as it is well illustrated in Fig.10b. We see, that the largest transverse flow can be generated at intermediate values of  $\phi_2$ . The limit of thin channel has recently been studied in details by using a general theory of mathematical bounds [68], and the optimum value of  $\phi_2 = 0.5$  corresponding a numerical example in Fig.10b has been rigorously derived [74].

An important conclusion from our analysis is that the surface textures which optimize transverse flow can significantly differ from those optimizing effective (forward) slip. It is well known, and we additionally demonstrated above, that the effective slip of a super-hydrophobic surface is maximized by reducing the solid-liquid area fraction  $\phi_1$ . In contrast, we have shown that transverse flow in super-hydrophobic channels is maximized by stripes with a rather large solid fraction,  $\phi_1 = 0.5$ , where the effective slip is relatively small.

## 7.2. Hydrodynamic interactions

As a consequence of the superlubrication potential, a hydrophobic texture could significantly modify squeeze film drainage between surfaces. It is of obvious practical interest to minimize the hydrodynamic resistance,  $F$ , to approach of surfaces.

For a Reynolds problem, where a disk of radius  $R$  is driven towards (in our case) a super-hydrophobic plane with a velocity  $U$  (see Fig. 11) we should solve Eqs.(3) by applying the effective tensorial boundary condition, Eq.(4), at the super-hydrophobic wall. This allows to derive a general expression for hydrodynamic pressure satisfying the condition  $p = p_0$  at the edge of the disk [75]

$$p = p_0 + \frac{U (R^2 - r^2)}{2 (C_x + C_y)}, \quad r^2 = x^2 + y^2, \quad (36)$$

where

$$C_x = \frac{H^3}{12\eta} \frac{H + 4b_{\text{eff}}^{\parallel}}{H + b_{\text{eff}}^{\parallel}} \quad C_y = \frac{H^3}{12\eta} \frac{H + 4b_{\text{eff}}^{\perp}}{H + b_{\text{eff}}^{\perp}} \quad (37)$$

The drag force may then be evaluated as the integral over the disk's surface and reads [75]

$$F = \frac{3\pi\eta UR^4}{2H^3} f_{\text{eff}}^* = F_R f_{\text{eff}}^*, \quad (38)$$

where  $F_R$  represents the classical solution of creeping flow equations of the Reynolds lubrication theory [76], and the correction for an effective slip is

$$f_{\text{eff}}^* = \frac{F}{F_R} = 2 \left[ \frac{H + 4b_{\text{eff}}^{\parallel}(H)}{H + b_{\text{eff}}^{\parallel}(H)} + \frac{H + 4b_{\text{eff}}^{\perp}(H)}{H + b_{\text{eff}}^{\perp}(H)} \right]^{-1}. \quad (39)$$

Thus the effective correction for a super-hydrophobic slip is the harmonic mean of corrections expressed through effective slip lengths in two principal directions,

$$f_{\text{eff}}^* = 2 \left( \frac{1}{f_{\text{eff}}^{*,\parallel}} + \frac{1}{f_{\text{eff}}^{*,\perp}} \right)^{-1} \quad (40)$$

In case of isotropic textures, all directions are equivalent with  $b_{\text{eff}}^{\parallel} = b_{\text{eff}}^{\perp} = b_{\text{eff}}$ , so we get

$$f_{\text{eff}}^* = \frac{F}{F_R} = \frac{H + b_{\text{eff}}(H)}{H + 4b_{\text{eff}}(H)} \quad (41)$$

Obviously, the case  $b_{\text{eff}}^{\parallel} = b_{\text{eff}}^{\perp} = 0$  corresponds to  $f_{\text{eff}}^* = 1$  and gives the Reynolds formula.

The expression for  $f_{\text{eff}}^*$  is very general and relates it to the effective slip length of the super-hydrophobic wall and the gap. In order to quantify the reduction of a drag force due to a presence of a super-hydrophobic wall, this expression can be used for *all* anisotropic and isotropic textures, where analytical or numerical expressions for  $b_{\text{eff}}^{\parallel,\perp}$  have been obtained.

An important consequence of Eq.(39) is that to reduce a drag force we need to maximize the ratio  $b_{\text{eff}}/H$ , but not the absolute values of effective slip itself. This is illustrated in Fig. 12a, where values presented in Fig. 8b were used to compute the correction for effective slip,  $f_{\text{eff}}^*$  as a function of the gap. At small  $H/L$  our calculations reproduce the asymptotic values predicted by Eqs. (20). They however vanish at large distances, where  $b_{\text{eff}}^{\parallel,\perp}/H$  are getting negligibly small. The useful analytical expressions for  $f_{\text{eff}}^*$  corresponding to a configuration of stripes are presented in Table 2. Similar estimates for the most important situation of a thin gap can similarly be done for some isotropic textures, and we include these results into Table 3.

The results presented in Tables 2 and 3 suggest that the key parameter determining reduction of drag is the area fraction of gas,  $\phi_2$ , in contact with the liquid. This is illustrated in Fig. 12b, where (using a relatively large  $b/H$ ) Hashin-Strickman bounds for  $f_{\text{eff}}^*$  are plotted versus  $\phi_2$ . If this is very small (or  $\phi_1 \rightarrow 1$ ) for all textures, the correction for slip tends to its absolute maximum,  $f_{\text{eff}}^* \rightarrow 1$ . In the most interesting

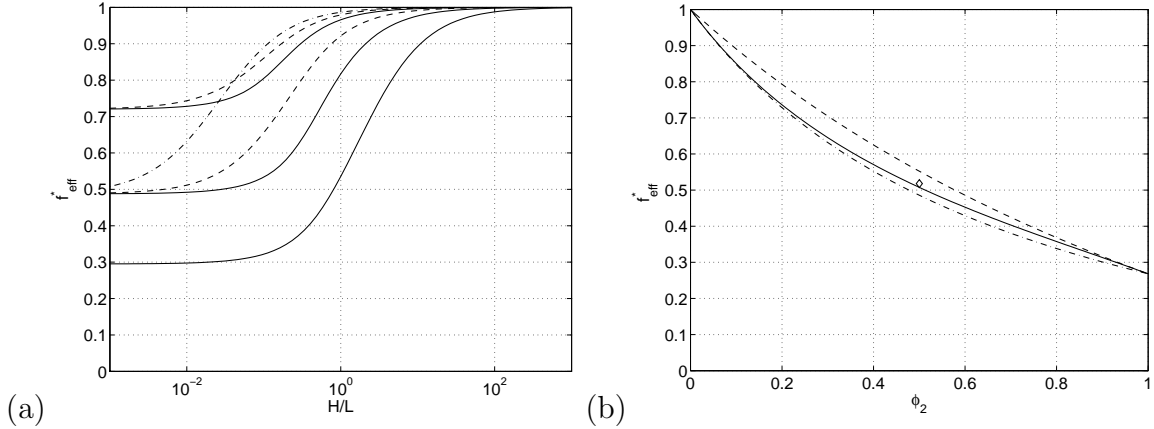


**Figure 12.** (a) The correction factor  $f_{\text{eff}}^* = F/F_R$  for hydrodynamic resistance force exerted on disk interacting with super-hydrophobic stripes vs. dimensionless gap width  $H/L$ . Solid curves correspond to local slip length  $b/L = 10$  (from top to bottom  $\phi_2 = 0.2, 0.5$  and  $0.9$ ), dashed curves – to  $b/L = 0.1$  (from top to bottom  $\phi_2 = 0.2$  and  $0.5$ ), dash-dotted curve - to  $b/L = 0.01$  and  $\phi_2 = 0.5$ . (b) The plot of  $f_{\text{eff}}^*$  versus  $\phi_2$  for a thin gap ( $H \ll L$ ) and several super-hydrophobic patterns: anisotropic stripes (solid line), isotropic textures attaining Hashin-Strickman bounds (dashed and dash-dotted lines) and isotropic Schulgasser structure (diamond), all with local slip  $b/H = 10$ .

**Table 2.** Asymptotic expansions for the force correction factor  $f_{\text{eff}}^*$  in case of a striped surface

Limiting case	$f_{\text{eff}}^*$
$H \gg \max\{L, b\}$	$1 - \frac{3(b_{\text{eff}}^{\parallel} + b_{\text{eff}}^{\perp})}{2H}$
$L \ll H \ll b$	$\frac{1}{4} + \frac{9}{32L} \frac{\pi H}{\ln(\sec(\pi\phi_2/2))}$
$b \ll H \ll L$	$1 - \frac{3b\phi_2}{H}$
$H \ll \min\{L, b\}$	$\frac{2(4 - 3\phi_2)}{8 + 9\phi_2 - 9\phi_2^2}$

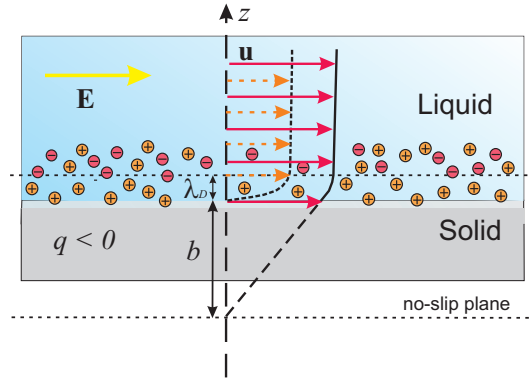
limit,  $\phi_2 \rightarrow 1$ , we can achieve the minimum possible value of correction for effective slip,  $f_{\text{eff}}^* \rightarrow 1/4$  provided  $b/H$  is large enough. We also stress that the results for stripes are confined between Hashin-Strickman bounds for  $f_{\text{eff}}^*$ . In other words, isotropic textures might be the best candidates for a reduction of a drag force.

## 8. Electro-osmotic flow over super-hydrophobic surfaces

Electro-osmosis, i.e. flow generation by an electric field, represents an example of interfacially driven flows [65] which are currently are intensively used in microfluidics. It may be enhanced by surface slippage, even for nanometric slip length. The reason for

**Table 3.** Correction factor  $f_{\text{eff}}^*$  for some specific isotropic patterns in a thin gap limit

Pattern	$b \ll H \ll L$	$H \ll \min\{L, b\}$
Hashin-Strickman upper bound	$1 - \frac{3b\phi_2}{H}$	$\frac{5 - 3\phi_2}{5 + 3\phi_2}$
Hashin-Strickman lower bound	$1 - \frac{3b\phi_2}{H}$	$\frac{8 - 3\phi_2}{4(2 + 3\phi_2)}$
Phase interchange textures	$1 - \frac{3b}{2H}$	$\frac{1}{2}$

**Figure 13.** Sketch of the influence of slippage on the electro-osmotic flow.

this amplification is that the electric double layer (EDL), characterized by the Debye screening length  $\lambda_D = \kappa^{-1}$  defines an additional length scale of the problem comparable to  $b$ . According to classical formula [77, 78]

$$u = -\frac{q_0 E_0}{\eta \kappa} (1 + b\kappa) \quad (42)$$

where  $u$  is the electro-osmotic velocity (outside of the double layer),  $q_0$  is the surface charge density, and  $E_0$  is the tangential electric field. Therefore, the flow can potentially be enhanced for a thin compared to  $b$  EDL, i.e. when  $\kappa b \gg 1$  (see Fig. 13).

For this reason, it is attractive to consider electro-osmotic flow over super-hydrophobic surfaces, whose texture can significantly amplify hydrodynamic slip. Eq.(42) suggests that a massive amplification of electro-osmotic flow can be achieved over super-hydrophobic surfaces. However, the controlled generation of such flows is by no means obvious since both the slip length and a charge distribution are inhomogeneous and anisotropic. Despite its fundamental and practical significance, electro-osmotic flow over super-hydrophobic surface has received little attention.

Recently, such a flow has been investigated past inhomogeneously charged slipping surface in the case of a thick channel ( $H \gg L$ ) and perfect slip ( $b \rightarrow \infty$ ) at the gas sectors [79, 80]. The summary of results for a case of stripes presented in is given in table 4 and we comment below on some useful limiting situations. Note that here we have

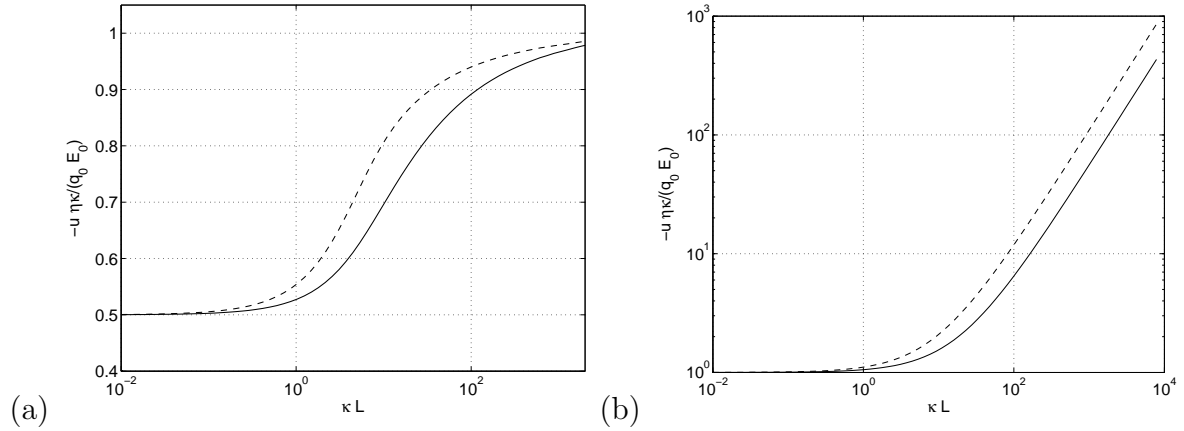


**Figure 14.** The electro-osmotic slip velocities for eigendirections of super-hydrophobic stripes ( $\phi_2 = 0.5$  and  $b/L \gg 1$ ) for (a) for uncharged gas sectors  $q_1 = q_0$ ,  $q_2 = 0$ , and (b) for a surface of a constant charge  $q_1 = q_2 = q_0$ . Solid curves correspond to transverse, and dashed - to longitudinal EO flow.

corrected erroneous expressions for a transverse electro-osmotic velocity given in [80]. The details of our analysis will be described elsewhere. For a thin EDL ( $\kappa L \gg 1$ ) no flow enhancement is predicted in case of uncharged gas interface [79], which has been confirmed by molecular dynamic simulations [81] and later analysis [80]. For uncharged gas interface with thick EDL ( $\kappa L \ll 1$ ), the results are qualitatively different. However, since  $\kappa L$  is small and since the electro-osmotic velocity become proportional to  $\phi_1$ , electro-osmotic flow becomes suppressed despite a large effective slip (see Fig. 14a). One main conclusion is that a charged gas interface is required to achieve an enhancement of electro-osmotic flow. For a uniformly charged anisotropic super-hydrophobic surface the electro-osmotic mobility can exhibit a large enhancement from effective hydrodynamic slip, possibly by an order of magnitude (see Fig. 14b).

In future, we suggest as a fruitful direction to consider electro-osmotic flow in a thin gap and by assuming a partial slip at the gas sectors. If similar relations hold for thin channels, then our results for the effective hydrodynamic slip suggest that transverse electrokinetic phenomena could be greatly amplified by using striped super-hydrophobic surfaces.

## 9. Conclusion

With recent progress in micro- and nanofluidics new interest has arisen in determining forms of hydrodynamic boundary conditions [3, 14, 16]. In particular, advances in lithography to pattern substrates have raised several questions in the modeling of the liquid motions over these surfaces and led to the concept of the effective tensorial slip. These effective conditions capture complicated effects of surface anisotropy and can be used to quantify the flow over complex textures without the tedium of enforcing real inhomogeneous boundary conditions.



**Table 4.** Electroosmotic slip past super-hydrophobic stripes

<i>General results</i> ( $\langle q \rangle = \phi_1 q_1 + \phi_2 q_2$ )		
	Thin EDL ( $\kappa L \gg 1$ )	Thick EDL ( $\kappa L \ll 1$ )
$u_{\parallel}$	$-\frac{E_0}{\eta\kappa} \left( q_1 + q_2 \frac{\kappa L}{\pi} \ln \left[ \sec \left( \frac{\pi\phi_2}{2} \right) \right] \right)$	$-\frac{\langle q \rangle E_0}{\eta\kappa} \left( 1 + \frac{\kappa L}{\pi} \ln \left[ \sec \left( \frac{\pi\phi_2}{2} \right) \right] \right)$
$u_{\perp}$	$-\frac{E_0}{\eta\kappa} \left( q_1 + q_2 \frac{\kappa L}{2\pi} \ln \left[ \sec \left( \frac{\pi\phi_2}{2} \right) \right] \right)$	$-\frac{\langle q \rangle E_0}{\eta\kappa} \left( 1 + \frac{q_2 \kappa L}{\langle q \rangle 2\pi} \ln \left[ \sec \left( \frac{\pi\phi_2}{2} \right) \right] \right)$
<i>Uncharged liquid-gas interface</i> ( $q_1 = q_0, q_2 = 0$ )		
	Thin EDL	Thick EDL
$u_{\parallel}$	$-\frac{E_0 q_0}{\eta\kappa}$	$-\frac{\phi_1 q_0 E_0}{\eta\kappa} \left( 1 + \frac{\kappa L}{\pi} \ln \left[ \sec \left( \frac{\pi\phi_2}{2} \right) \right] \right)$
$u_{\perp}$	$-\frac{E_0 q_0}{\eta\kappa}$	$-\frac{\phi_1 q_0 E_0}{\eta\kappa}$
<i>Charged liquid-gas interface</i> ( $q_1 = q_2 = q_0$ )		
	Thin EDL	Thick EDL
$u_{\parallel}$	$-\frac{E_0 q_0}{\eta\kappa} \left( 1 + \frac{\kappa L}{\pi} \ln \left[ \sec \left( \frac{\pi\phi_2}{2} \right) \right] \right)$	$-\frac{q_0 E_0}{\eta\kappa} \left( 1 + \frac{\kappa L}{\pi} \ln \left[ \sec \left( \frac{\pi\phi_2}{2} \right) \right] \right)$
$u_{\perp}$	$-\frac{E_0 q_0}{\eta\kappa} \left( 1 + \frac{\kappa L}{2\pi} \ln \left[ \sec \left( \frac{\pi\phi_2}{2} \right) \right] \right)$	$-\frac{q_0 E_0}{\eta\kappa} \left( 1 + \frac{\kappa L}{2\pi} \ln \left[ \sec \left( \frac{\pi\phi_2}{2} \right) \right] \right)$

This work has discussed the issue of boundary conditions at smooth hydrophobic and rough hydrophilic surfaces, and has then given the especial emphasis to the derivation of effective boundary conditions for a flow past hydrophobic solid surfaces with special textures that can exhibit greatly enhanced ('super') properties, compared to analogous flat or slightly disordered surfaces [5]. After a decade of intense research there have been hundreds of materials developed and some macroscopic applications (such as self-cleaning, for example), but there is still no real small scale applications (for example, in micro- and nanofluidics).

We have derived accurate formulas describing effective boundary conditions for pressure-driven flow past super-hydrophobic textures of special interest (such as stripes, fractal patterns of nested circles, chessboards, and more). We have analyzed both thin (compared to texture characteristic length) and thick channel situations, and in some cases (e.g. periodic stripes) have obtained exact solutions valid for an arbitrary thickness of the channel. The predicted large effective slip of super-hydrophobic surfaces compared

to simple, smooth channels can greatly lower the viscous drag of thin microchannels.

The power of the tensor formalism and the concept of effective slippage was then demonstrated by exact solutions for two other potential applications: optimization of the transverse flow and analytical results for the hydrodynamic resistance to approach of two surfaces. These examples demonstrate that properly designed super-hydrophobic surfaces could generate a very strong transverse flow and significantly reduce the so-called ‘viscous adhesion’. A striking conclusion from our analysis is that the surface textures which optimize transverse flow or thin film drainage can significantly differ from those optimizing effective (forward) slip. Finally, we have discussed how super-hydrophobic surfaces could amplify electrokinetic pumping in microfluidic devices.

As we see, a combination of wetting and roughness provides many new and very special hydrodynamic properties of surfaces, which could be explored with the formalism discussed here. We hope our analysis will allow the local slip tensors to be determined by global measurements, such as the permeability of a textured channel as a function of the surface orientations or the hydrodynamic force exerted on the body approaching a super-hydrophobic plates. They may also guide the design of super-hydrophobic surfaces for microfluidic lab-on-a-chip and other applications.

## Acknowledgments

This research was supported by the DFG through its priority programme ‘Micro- and nanofluidics’ and by the RAS through its priority program ‘Assembly and Investigation of Macromolecular Structures of New Generations’.

## References

- [1] Batchelor G K 2000 *An Introduction to Fluid Dynamics* (Cambridge University Press)
- [2] Squires T M and Quake S R 2005 *Reviews of Modern Physics* **77** 977
- [3] Stone H A, Stroock A D and Ajdari A 2004 *Annual Review of Fluid Mechanics* **36** 381
- [4] Vinogradova O I 1999 *Int. J. Miner. Proc.* **56** 31
- [5] Quere D 2005 *Rep. Prog. Phys.* **68** 2495
- [6] Vinogradova O I 1995 *Langmuir* **11** 2213
- [7] Vinogradova O I 1995 *J. Colloid Interface Sci.* **169** 306
- [8] Lauga E, Brenner M P and Stone H A 2007 *Handbook of Experimental Fluid Dynamics* chap. 19, 1219–1240 (NY: Springer)
- [9] Bocquet L and Barrat J L 2007 *Soft Matter* **3** 685
- [10] Huang D, Sendner C, Horinek D, Netz R and Bocquet L 2008 *Phys. Rev. Lett.* **101** 226101
- [11] Sendner C, Horinek D, Bocquet L and Netz R 2009 *Langmuir* **25** 10768
- [12] Andrienko D, Dünweg B and Vinogradova O I 2003 *J. Chem. Phys.* **119** 13106
- [13] Dammler S M and Lohse D 2006 *Phys. Rev. Lett.* **96** 206101
- [14] Bazant M Z and Vinogradova O I 2008 *J. Fluid Mech.* **613** 125
- [15] Feuillebois F, Bazant M Z and Vinogradova O I 2009 *Phys. Rev. Lett.* **102** 026001
- [16] Kamrin K, Bazant M and Stone H A 2010 *J. Fluid Mech.* **658** 409
- [17] Quere D 2008 *Annu. Rev. Mater. Res.* **38** 71
- [18] Chan D and Horn R 1985 *J. Chem. Phys.* **83** 5311
- [19] Cottin-Bizonne C, Cross B, Steinberger A and Charlaix E 2005 *Phys. Rev. Lett.* **94** 056102

- [20] Horn R G, Vinogradova O I, Mackay M E and Phan-Thien N 2000 *J. Chem. Phys.* **112** 6424
- [21] Vinogradova O I and Yakubov G E 2003 *Langmuir* **19** 1227
- [22] Vinogradova O I 1996 *Langmuir* **12** 5963
- [23] Pit R, Hervet H and Leger L 2000 *Phys. Rev. Lett.* **85** 980
- [24] Trethewey D C and Meinhart C D 2002 *Phys. Fluids* **14** L9
- [25] Joseph P and Tabeling P 2005 *Phys. Rev. E* **71** 035303(R)
- [26] Huang P, Guasto J and Breuer K 2006 *J. Fluid Mech.* **566** 447
- [27] Zettner C and Yoda M 2003 *Experiments in Fluids* **34** 115
- [28] Li H, Sadr R and Yoda M 2006 *Experiments in Fluids* **41** 185
- [29] Vinogradova O I, Koynov K, Best A and Feuillebois F 2009 *Phys. Rev. Lett.* **102** 118302
- [30] Lumma D, Best A, Gansen A, Feuillebois F, Rädler J O and Vinogradova O I 2003 *Phys. Rev. E* **67** 056313
- [31] Joly L, Ybert C and Bocquet L 2006 *Phys. Rev. Lett.* **96** 046101
- [32] Yordanov S, Best A, Butt H J and Koynov K 2009 *Optics Express* **17** 21150
- [33] Rothstein J P 2010 *Annu. Rev. Fluid Mech.* **42** 89
- [34] Neto C, Evans D, Bonaccorso E, Butt H J and Craig V J 2005 *Rep. Prog. Phys.* **68** 2859
- [35] Bocquet L and Charlaix E 2010 *Chem. Soc. Rev.* **39** 1073
- [36] Kunert C, Harting J and Vinogradova O I 2010 *Phys. Rev. Lett* **105** 016001
- [37] Thompson P A and Troian S M 1997 *Nature* **389** 360
- [38] Harting J, Kunert C and Herrmann H 2006 **75** 328
- [39] Vinogradova O I and Yakubov G E 2006 *Phys. Rev. E* **73** 045302(R)
- [40] Honig C D F and Ducker W A 2007 *Phys. Rev. Lett.* **98** 028305
- [41] Bouzigues C I, Tabeling P and Bocquet L 2008 **101** 114503
- [42] Maali A, Hurth C, Cohen-Bouhacina T, Gouturier G and Aime J P 2006 *Appl. Phys. Lett.* **88** 163504
- [43] Barrat J L and Bocquet L 1999 *Phys. Rev. Lett.* **82** 4671
- [44] Vinogradova O I, Bunkin N F, Churaev N V, Kiseleva O A, Lobeyev A V and Ninham B W 1995 *J. Colloid Interface Sci.* **173** 443
- [45] Yakubov G E, Butt H J and Vinogradova O I 2000 *J. Phys. Chem. B* **104** 3407
- [46] Borkent B, Dammmer S, Schonherr H, Vansco G and Lohse D 2007 *Phys. Rev. Lett.* **98** 204502
- [47] Ishida N, Inoue T, Miyahara M and Higashitani K 2000 *Langmuir* **16** 6377
- [48] Bonaccorso E, Butt H J and Craig V S J 2003 *Phys. Rev. Lett.* **90** 144501
- [49] Granick S, Zhu Y and Lee H 2003 *Nat. Mater.* **2** 221
- [50] Zhu Y X and Granick S 2002 *Phys. Rev. Lett.* **88** 106102
- [51] Sarkar K and Prosperetti A 1996 *J. Fluid Mech.* **316** 223
- [52] Lecoq N, Anthore R, Cichocki B, Szymczak P and Feuillebois F 2004 *J. Fluid Mech.* **513** 247
- [53] Kunert C and Harting J 2007 *Phys. Rev. Lett* **99** 176001
- [54] Ybert C, Barentin C, Cottin-Bizonne C, Joseph P and Bocquet L 2007 *Phys. Fluids* **19** 123601
- [55] Belyaev A V and Vinogradova O I 2010 *J. Fluid Mech.* **652** 489
- [56] Cottin-Bizonne C, Barentin C, Charlaix E, Bocquet L and Barrat J L 2004 *Eur. Phys. J. E* **15** 427
- [57] Cottin-Bizonne C, Barrat J L, Bocquet L and Charlaix E 2003 *Nat. Mater.* **2** 237
- [58] Hyväluoma J and Harting J 2008 *Phys. Rev. Lett.* **100** 246001
- [59] Davis A M J and Lauga E 2009 *Phys. Fluids* **21** 011701
- [60] Sbragaglia M and Prosperetti A 2007 *Phys. Fluids* **19** 043603
- [61] Pirat C, Sbragaglia M, Peters A M, Borkent B M, Lammertink R G H, Wessling M and Lohse D 2008 *Europhys. Lett.* **81** 6602
- [62] Reyssat M, Yeomans J M and Quere D 2008 *Europhys. Lett.* **81** 26006
- [63] Ajdari A 2002 *Phys. Rev. E* **65** 016301
- [64] Stroock A D, Dertinger S K, Whitesides G M and Ajdari A 2002 *Anal. Chem.* **74** 5306
- [65] Ajdari A and Bocquet L 2006 *Phys. Rev. Lett.* **96** 186102

- [66] Lauga E and Stone H A 2003 *J. Fluid Mech.* **489** 55
- [67] Batchelor G K 1970 *J. Fluid Mech.* **44** 419
- [68] Torquato S 2002 *Random Heterogeneous Materials: Microstructure and Macroscopic Properties* (Springer)
- [69] Feuillebois F, Bazant M Z and Vinogradova O I 2010 *Phys. Rev. Lett.* **104** 159902
- [70] Stroock A D, Dertinger S K W, Ajdari A, Mezić I, Stone H A and Whitesides G M 2002 *Science* **295** 647
- [71] Wang C Y 2003 *Physics of Fluids* **15** 1114
- [72] Stroock A D and McGraw G J 2004 *Philosophical Transactions of the Royal Society A* **04TA1803**  
1
- [73] Ou J, Moss J M and Rothstein J P 2007 *Phys. Rev. E* **76** 016304
- [74] Feuillebois F, Bazant M Z and Vinogradova O I 2010 *Phys. Rev. E* **82** 055301 (R)
- [75] Belyaev A V and Vinogradova O I 2010 *Soft Matter* **6** 4563
- [76] Reynolds O 1886 *Philos. Trans. R. Soc. London* **177** 157
- [77] Joly L, Ybert C, Trizac E and Bocquet L 2004 *Phys. Rev. Lett.* **93** 257805
- [78] Muller V M, Sergeeva I P, Sobolev V D and Churaev N V 1986 *Colloid J. USSR* **48** 606
- [79] Squires T M 2008 *Phys. Fluids* **20** 092105
- [80] Bahga S S, Vinogradova O I and Bazant M Z 2010 *J. Fluid Mech.* **644** 245
- [81] Huang D M, Cottin-Bizzone C, Ybert C and Bocquet L 2008 *Phys. Rev. Lett.* **101** 064503